Linear magnetoelectric memory and training effect in the honeycomb antiferromagnet $Co_4Nb_2O_9$

Yuting Chang,[1] Junfeng Wang,[1] Wei Wang,[1] Congbin Liu,[2] Bin You,[1] Meifeng Liu,[3] Shuhan Zheng,[3,4] Mengyi Shi,[1] Chengliang Lu,[1,*] and Jun-Ming Liu[3,4]

[1]*School of Physics & Wuhan National High Magnetic Field Center, Huazhong University of Science and Technology, Wuhan 430074, China*

[2]*College of Physics and Electronic Engineering, Nanyang Normal University, Nanyang 473061, China*

[3]*Institute for Advanced Materials, Hubei Normal University, Huangshi 435001, China*

[4]*Laboratory of Solid State Microstructures, Nanjing University, Nanjing 210093, China*

(Received 7 November 2021; revised 25 November 2022; accepted 9 January 2023; published 17 January 2023)

We report observation of ultrarobust linear magnetoelectric memory and significant training effect in a honeycomb antiferromagnet $Co_4Nb_2O_9$, which is controllable by magnetic and electric fields. The memory states show distinct linear magnetoelectric coefficients over a broad magnetic field range. Antiferromagnetic domain evolution is believed to be responsible for the versatile memory behaviors promisingly accessible in multiferroics and other magnetoelectric materials such as topological insulators. The compensated antiferromagnetic phase essential to the magnetoelectric memory may allow to further integrate the unique merits of antiferromagnetic spintronics such as ultrahigh density and ultrafast switching.

DOI: 10.1103/PhysRevB.107.014412

I. INTRODUCTION

Magnetoelectrics provide a fertile ground for studying the intrinsic coupling between electric polarization (P) and magnetization (M), which has been the center of attention in condensed-matter physics due to the fascinating fundamental physics and potential applications in such as low-energy dissipative data storage [1–3]. The magnetoelectric (ME) coupling is usually described using Landau theory which contains many terms of the twisting of ferroic orders with external fields: $P_i = \alpha_{ij}H_j + \beta_{ijk}H_jH_k/2 + \ldots$ (or $\mu_0 M_j = \alpha_{ij}E_i + \gamma_{jik}E_iE_k/2 + \ldots$), where α_{ij}, β_{ijk}, and γ_{jik} are ME coupling tensors, and H and E are magnetic and electric fields, respectively [4–7]. Probably due to the motivation of combining the best aspects of ferroelectric and magnetic memories, previous studies have mainly focused on the primary ferroic-order parameters P and M, but much less explored the merit of magnetoelectricity. Simply looking at the ME equation suggests that the ME tensors would be equally important as other parameters. Another possible reason for such unbalanced interests may arise from the rather complicated ME behaviors due to the mixed terms in the majority of magnetoelectrics [1]. Despite these facts, ME memory using the coefficient has been observed in composite material, and utilized to mimic neural network [8,9], which is impressive especially for the cross control of P (M) with H (E). Recently, Kosub *et al.* revealed remarkable reduction of writing threshold in a random access memory device made of the paradigmatic linear ME material Cr_2O_3 [10].

Most studies of magnetoelectrics since the 60s of the last century were devoted to the linear ME effect, i.e., H causes variation in electric polarization or E induces magnetization. Benefiting from the intensive efforts, it has been revealed that the linear magnetoelectricity contains manifold basic contributions, i.e., electronic vs lattice response and spin vs orbital magnetic components, which may allow to tune the ME coupling efficiently. For instance, in Cr_2O_3, it was found that the transverse and longitudinal response are dominated by spin and orbital contributions, respectively, which are quite unique [11,12]. First principles calculations proposed that large orbital ME response may be obtained just by containing ions with large orbital moment in materials [13]. Moreover, emergent functionalities would be expected based on the simple association between the magnetic and electric variables. For instance, if the artificial neural network is based on linear ME instead of the nonlinear effect as observed in the ME composite systems [8,9], excellent accuracy would be achieved, which is in fact a core issue of the related activities [14,15].

However, it looks challenging to functionalize the linear magnetoelectricity, probably due to the zero spontaneous P at $H = 0$. There are to date just few examples of linear ME memory existing in literature [16–22]. This is intriguing, since there are a large variety of linear ME materials, and most of them (and also multiferroics) are antiferromagnetic (AFM). It is worth to mention that AFM spintronics host superior properties such as ultrafast spin dynamics and ultrahigh density due to the inherent zero stray field, which is factually a very active field in the present stage [23–25]. Moreover, symmetric exchange and asymmetric exchange are two major mechanisms for the generation of P in linear ME materials [7], similar to the type-II multiferroicity. Therefore, there would be no reason to see diverse memory phenomena in type-II multiferroics, but limited cases in linear magnetoelectrics. Especially, motivated by the uniqueness of linear ME coupling mentioned above, it is of high interest and actuality to search and understand memory effect based on linear magnetoelectricity.

*cllu@hust.edu.cn

In this work, we demonstrate nonvolatile memory enabled by linear ME coupling of compensated antiferromagnet $Co_4Nb_2O_9$, while this linear ME response can be controlled by both H and E. The memory states possess excellent linearity within a broad field range up to ~ 23 T. Significant training effect is observed, which is designable by the maximum applied H. Our results show that linear ME memory is not only accessible, but also can be more versatile in antiferromagnets.

II. EXPERIMENTS

$Co_4Nb_2O_9$ single crystals were grown by an optical floating-zone technique. The crystals were oriented using x-ray Laue photographs, and cut into thin plates with typical dimensions $\sim 2.3 \times 1 \times 0.2$ mm^3. Gold electrodes were sputtered on the widest surfaces (perpendicular to the [110] direction) of the samples before electric measurements. Before the high-field characterizations, some basic measurements such as M as a function of T and H were carried out with H applied along various crystalline directions using a superconducting quantum interference device (Quantum Design).

The high-field facilities in the Wuhan National High Magnetic Field Center were used. The measurements were carried out in pulsed magnetic fields up to 60 T with the pulse duration of $t \sim 11$ ms and $t \sim 90$ ms. Without special statements, the pulsed magnetic field with $t \sim 11$ ms was used for the measurements. Pulsed-field magnetization was measured by an induction method employing a couple of coaxial pickup coils. Two pulse shots with sample in and sample out were performed to subtract the spurious dB/dt signals. Then, dM/dt signals from the sample were collected and integrated as a function of magnetic field. The magnetoelectric current was measured as a voltage across a shunt resistor R_s. $R_s = 10$ kΩ is usually used, which is far smaller than the internal resistance of the sample (highly insulating at low temperature). The voltage across the shunt resistor R_s is probed using a measurement circuit, consisting of DC preamplifier, analog integrator, and analog-to-digital converters. By integrating the current with time, electric polarization as a function of H is obtained. The sample was first cooled from high temperature (far above $T_N \sim 27$ K) down to target temperature without applying magnetic field, and then the $I(H)$ measurements at different temperatures were carried out. During the electric measurements, a bias field $\pm E = 10$ kV/cm was applied. The interval between two high-field measurements is roughly 1–2 h. Magnetostriction effect along the [110] direction was measured with $H//[110]$ using an optical fiber grating method. The grating was bonded directly to the samples, which has the benefit of relative immunity from vibrations. The relative length change $\Delta L/L$ can be obtained from the shift of the Bragg wavelength of the grating.

III. RESULTS

$Co_4Nb_2O_9$ crystallizes in a trigonal symmetry, and Co^{2+} cations occupy two inequivalent sites, i.e., Co(1) and Co(2), as shown in Fig. 1(a) [26–28]. The $Co(1)O_6$ octahedra are corner linked while the $Co(2)O_6$ cages are edge shared, forming two different buckled honeycomb layers alternatively stacking along the c axis. $Co_4Nb_2O_9$ has a compensated AFM phase below $T_N \sim 27$ K, and the magnetic moments of Co are confined in the ab plane, i.e., an easy-plane magnetic anisotropy. According to recent neutron-scattering experiments [28,29], along the c axis, the nearest-neighbor Co(1) and Co(2) are ferromagnetically coupled, while the next-nearest neighbor Co(1) and Co(2) has a relative canting angle of $\sim 10.5^\circ$ at $H = 0$. In the Co(2) hexagonal rings with slight distortion, the magnetic moments of neighboring Co(2) ions are exactly antiparallel (or just show tiny relative canting). In the Co(1) rings which are highly distorted, the Co(1) magnetic moments display relatively canting within every hexagonal ring. The magnetic configurations of Co rings are schematically shown in the bottom of Fig. 1(a). There are two blocks, i.e., block a and block b, which stack alternatively along the c axis. It is expected to have plural domains in the system once the stacking is disturbed, e.g., -a-b-b-a- arrangement may emerge. Moreover, because of the trigonal lattice symmetry, the AFM domains can have various orientations.

While $M \sim 0$ is evidenced in the ground state, typical AFM characters are illustrated by the linear $M(H)$ curves with $H//[110]$ up to the highest field of ~ 52 T at $T = 4.2$ K [Fig. 1(b)]. The $M(H)$ data, shown in Fig. 1(b), find two additional anomalies at $\mu_0 H_{c1} \sim 23$ T and $\mu_0 H_{c2} \sim 41$ T. The weak kink feature in the dM/dH curve at H_{c1} may due to domain evolution, which is associated with the ME memory effect as described below. The transition at H_{c2} is sharp, with $M \sim 12.3\ \mu_B$/f.u. matching well with previous neutron data [28–30], suggesting the AFM to ferromagnetic (FM) transition where the Co-magnetic moments are totally switched to the FM alignment along [110]. As shown in Fig. 1(c), the magnetostriction reaches up to $\Delta L/L \sim 180$ ppm in the high-H range, where L and ΔL are the sample's length and its variation. Similar large magnetostriction was also revealed by Khanh *et al.* [31]. At $\mu_0 H_{c2} \sim 41$ T, $\Delta L/L$ turns to decrease with H, implying lattice contraction. Such lattice modulation would be essential for the development of domain walls. The smooth variation of $\Delta L/L(H)$ around $\mu_0 H_{c1} \sim 23$ T indicates that H_{c1} is due to domain evolution rather than phase transition.

More amazing is the emergence of H-driven nonzero P over the broad-H range, evidencing the linear ME effect expressed by $P = \alpha H$. The measured magnetocurrent I by varying $H//[110]]$ is plotted in Fig. 1(d) and the electric polarization data in Fig. 1(e). The magnetically driven P, based on the symmetry argument [32,33], has its major component along the [110] direction. The $I(H)$ data demonstrate distinctly different behaviors in various H ranges, as shown in Fig. 1(d). First, $I(H)$ appears to be a nonzero constant at $H < H_{c1}$ except the very small field window, the consequence of the linear ME effect. Second, the constant I values, respectively, in the H-increasing and H-decreasing sequences, as indicated by arrows imply different linear $P(H)$ dependences and thus different α values in the two sequences. Third, the two anomalies in the high-H range are identified in connection with the $M(H)$ data, evidencing that the ME effect is intrinsic.

Consequently, the evaluated $P(H)$ curves are plotted in Fig. 1(e). The most striking feature is the remarked $P(H)$ hysteresis with two distinct linear ME branches, i.e., the ME memory addressed in this work. The ME coefficient

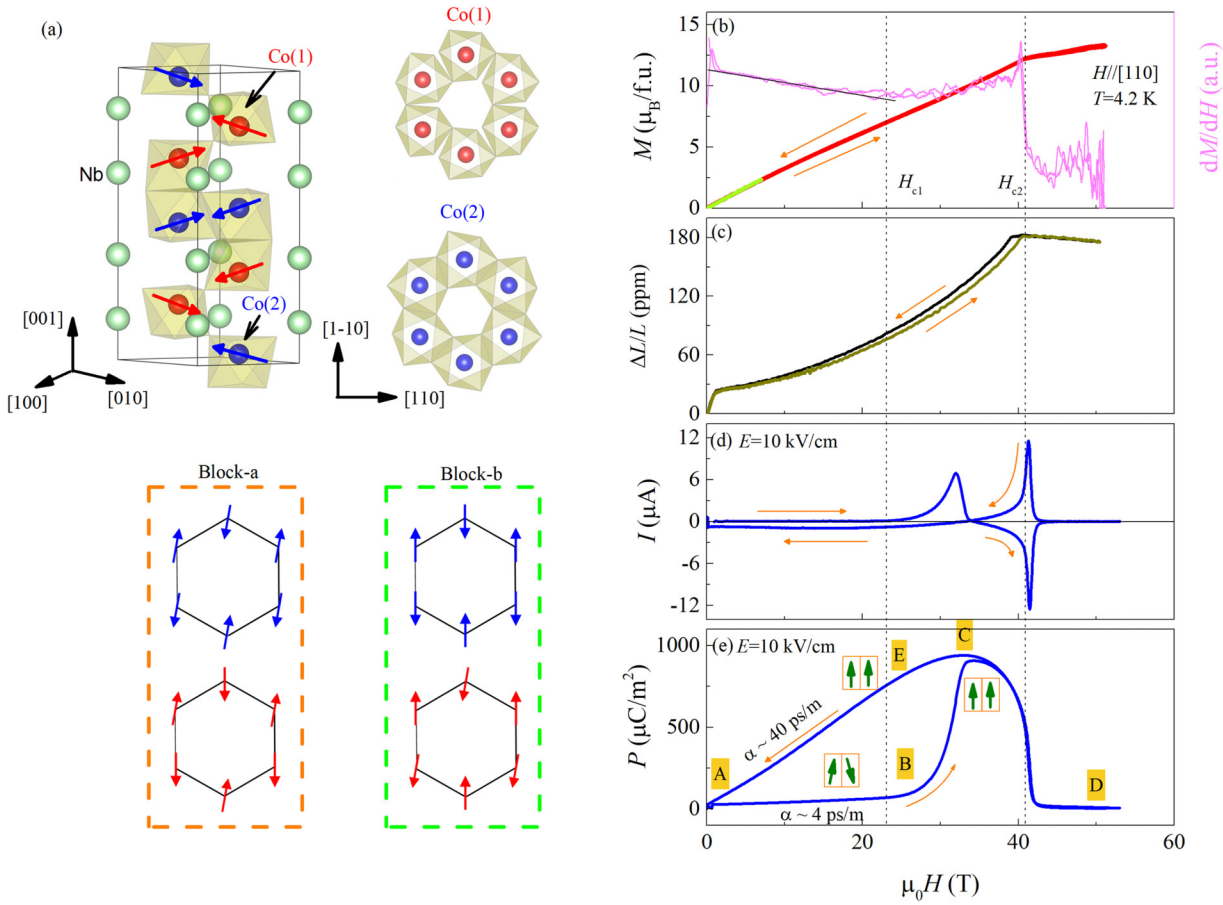

FIG. 1. (a) Sketches of crystalline and magnetic structures of $Co_4Nb_2O_9$, where the two inequivalent Co sites are labeled. Possible magnetic hexagonal rings are drawn at the bottom, and two blocks are indicated. (b) Magnetization as a function of $\mu_0 H$. The corresponding dM/dH data are also shown, and two anomalies can be identified at $\mu_0 H_{c1} \sim 23$ T and $\mu_0 H_{c2} \sim 41$ T. (c) Magnetostriction $\Delta L/L$ as a function of $\mu_0 H$. (d) Magnetoelectric current I as a function of $\mu_0 H$ measured with $E = 10$ kV/cm. (e) Integrated electric polarization P. The arrangement of P components is sketched (olive arrows). Marks A–E indicate the positions with different P. All the properties were measured with $H//[110]$ at $T = 4.2$ K.

$\alpha = dP/dH$ for the two linear ME states in the H-increasing and H-decreasing sequences (paths) are ~ 4 and ~ 40 ps/m, respectively. Obviously, the two distinct ME states are due to the drastically enhanced P event as $H > H_{c1}$, reaching the maximal at $\mu_0 H_{max} \sim 33$ T in the H-increasing sequence. The big difference in the two sequences originates from the AFM domain evolution, as discussed below.

As a ME memory, one of its advantages is the possible electrocontrol of memory states including ME response and AFM domain structure. To demonstrate this advantage, the sample was magnetically zero-field cooled down to $T = 4.2$ K, and the ME effect was measured under a given electric field $E = \pm 10$ kV/cm. The obtained $I(H)$ curves are shown in Fig. 2(a) in the H cycle, respectively. The measured two sets of $I(H)$ curves show the roughly opposite behaviors with similar qualitative features such as two anomalies at H_{c1} and H_{c2}. The E-controlled $I(H)$ sign reversal is clearly demonstrated. Subsequently, the evaluated $P(H)$ curves are symmetric with the $P = 0$ axis and the two sets of ME coefficient $\alpha(H)$ show the opposite signs, as shown in Fig. 2(b). In such sense, the dual controllability of the AFM ME memory by both H and E is revealed.

Further, specifically designed experiments show that the ME memory is nonvolatile and interswitchable, shown in Fig. 3 as an examples. The initial state was obtained simply by zero magnetic-field cooling of the sample from far above T_N down to $T = 4.2$ K at which the measurement was performed. The [110]-oriented H with magnitude H_0 was applied to the

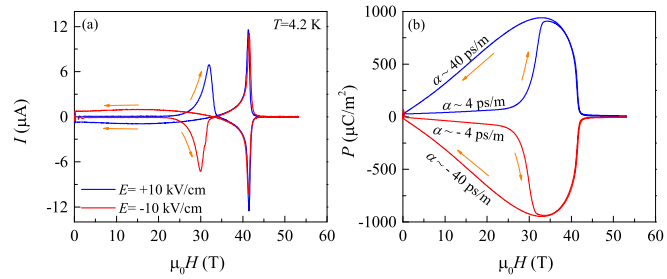

FIG. 2. (a) Magnetoelectric current I as a function of $\mu_0 H$ measured with $\pm E = 10$ kV/cm at $T = 4.2$ K. (b) Corresponding $P(H)$ curves are shown, which can be completely reversed by electric field. ME coefficients α are also labeled with the $P(H)$ curves.

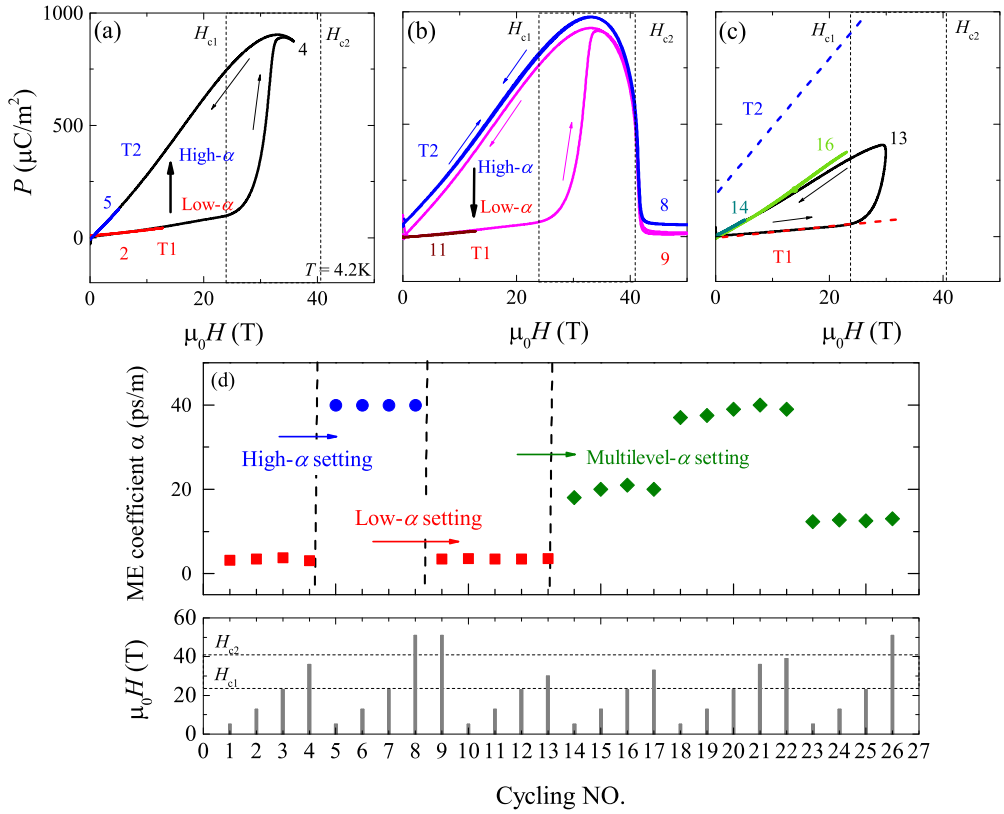

FIG. 3. Series of $P(H)$ curves obtained with different H cycles at $E = 10$ kV/cm and $T = 4.2$ K. Measurements were performed continuously. For clarity, only typical $P(H)$ curves are shown, and cycle 8 is offset vertically by 50 μC/m^2. (a) Low- to high-α setting. (b) High- to low-α setting. (c) Intermediate-α setting. Blue and red dashed lines indicate the T2 and T1 traces, respectively. (d) Summarized ME switching behaviors. Magnetic field for each H cycle is shown in the bottom figure.

sample in the H-increasing (decreasing) cycling as a writing (switching) process, while the resultant state is read out by a small H subsequently. For clarity, only typical data are shown here (the full data in the Supplemental Material [34]), and some $P(H)$ curves are shifted vertically.

(i) For a writing with $H_0 < H_{c1}$ (e.g., cycle 2) from the initial state, the measured $P(H)$ data always follow the T1 trace and exhibit no remarkable hysteresis, giving rise to a small $\alpha \sim 4$ ps/m, i.e., the sample is in the low-ME state.

(ii) For a writing with $H_0 > H_{c2}$ (e.g., cycles 8 and 9), no matter how the previous state is, the resultant state after the H cycling is the low-ME state with $\alpha \sim 4$ ps/m, i.e., the sample is written into the low-ME state. This may be due to domain redistribution after H cycle with $H_0 > H_{c2}$. Nevertheless, the measured $P(H)$ hysteresis depends on the previous ME state. For cycle 8, the $P(H)$ hysteresis shows no loop since the previous state is in the high-ME state ($\alpha \sim 40$ ps/m). For cycle 9, the $P(H)$ hysteresis shows large loop since the previous state is in the low-ME state ($\alpha \sim 4$ ps/m) after cycle 8.

(iii) For a writing with $H_0 \sim H_{max}$ at 4.2 K (e.g., cycle 4), no matter how the previous state is, the resultant state after the H cycling is the high-ME state with $\alpha \sim 40$ ps/m, i.e., the sample is written into the high-ME state.

The aforementioned low (high) ME-state writing sequences are all deterministic basically, which originates from the AFM domain evolution as described in the Supplemental Material [34]. Beyond this, history-dependent training effect is also observed, which occurs in the $H_{c1} < H_0 < H_{c2}$ region. For convenience, we start again from a different initial state, and our observations can be highlighted as the following:

(a) For cycling with $H_{c1} < H_0 < H_{max}$, the training sequences starting from a low-ME state are shown in Fig. 4(a) at $\mu_0 H_0 = 30$ T. This effect is characterized by the gradually shrinking $P(H)$ loop upon the sequential H cycling, accompanied with the gradual increasing of the ME coefficient from $\alpha \sim 4$ ps/m to $\alpha \sim 40$ ps/m, as demonstrated by the dependence of α on the cycling number [Fig. 4(c)]. Certainly, this number for completing the training process depends on H_0, and the more the cycling number the closer H_0 is to H_{c1}. It is expected that this number would be an exponential function of $(H_0–H_{c1})^{-1}$, typical for behaviors around a critical point.

(b) For cycling with $H_{max} < H_0 < H_{c2}$, the training behavior is somehow different, and the results are shown in Fig. 4(b) for $\mu_0 H_0 = 39$ T as an example. Here one sees switching from the high-ME state to an intermediate-ME state with reduced $\alpha \sim 13$ ps/m, accompanied by enlarged $P(H)$ loop. This ME state behaves quite stable against consecutive cycling with $\mu_0 H_0 = 39$ T (more data in the Supplemental Material [34]), different from the case with $\mu_0 H_0 = 30$ T. Such difference would be expectable since $\mu_0 H_0 = 39$ T is much larger than $\mu_0 H_{max}$, large enough to rewrite the ferroelectric and AFM state evidently. The training effect becomes significant as H_0 is closer to H_{c2}, while it becomes extremely slow if $H_0 \sim H_{max}$ where the system is always in the high-ME state.

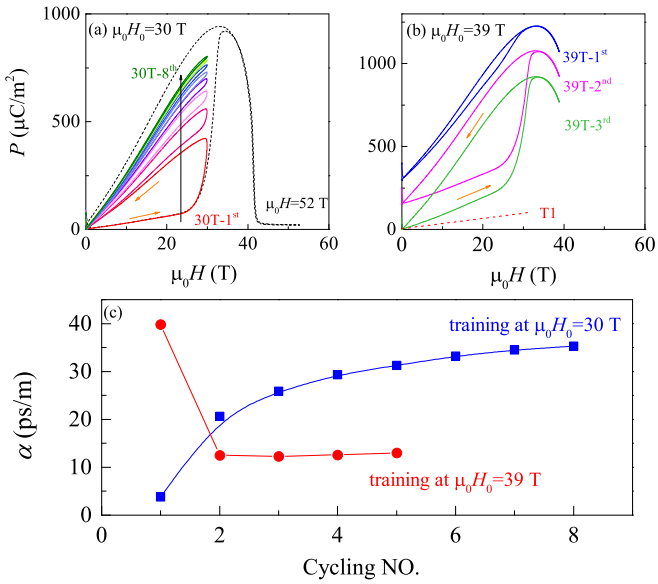

FIG. 4. (a) Starting from the low-α state, successive $P(H)$ curves were measured with $\mu_0 H_0 = 30$ T. (b) $P(H)$ curves obtained by continuous cycles with $\mu_0 H_0 = 39$ T. For clarity, the curves are offset vertically with a constant interval of 150 μC/m^2. (c) α as a function of H-cycling number. $E = 10$ kV/cm was applied during the measurements.

IV. DISCUSSION

The above experimental results have demonstrated linear ME memory in the compensated antiferromagnet $Co_4Nb_2O_9$, which is nonvolatile, ultrarobust, and controllable using H and E. In comparison with the traditional memory effect depending on the remnant magnetization and electric polarization [16–19], here the linear ME memory occurring in an antiferromagnet with $M = 0$ and $P = 0$ at $H = 0$ looks far more striking. The nonvolatile memory and training effect are quite reproducible in different samples which were cut from a big single-crystal rod. Surely our work just gives a proof of principle demonstration of ME memory using linear magnetoelectricity, and there is much room to improve the functionalities of such a device; in particular, the operation field can be optimized to achieve a more efficient writing process.

Although the microscopic origin of the spin-driven P in $Co_4Nb_2O_9$ remains unclear, the linear ME memory can be understood by the domain evolution in a qualitative sense. In Fig. 5(a), two possible arrangements of the Co rings are schematically drawn, e.g., domain-1 (-a-b-a-b-) and domain-3 (-b-a-b-a-), and at the domain walls (i.e., -a-b-b-a-) the exchange coupling are broken. The previous study has revealed that the relative canting between next-neighboring Co ions [also the neighboring Co(2) rings] along the c axis is quite robust, and just shows slight decrease from 10.5° to 8.5° when H is increased from 0 to 10 T [28]. This is probably due to the relatively large Dzyaloshinskii-Moriya interaction in $Co_4Nb_2O_9$, which is comparable with the primary exchange interactions [29]. Based on these results, block a′ and block b′, and the related domain 2 (-a′-b′-a′-b′) and domain 4 (-b′-a′-b′-a′-) due to different stacking of the blocks under $\mu_0 H > 0$ T can be drawn in Fig. 5(b), where the relative

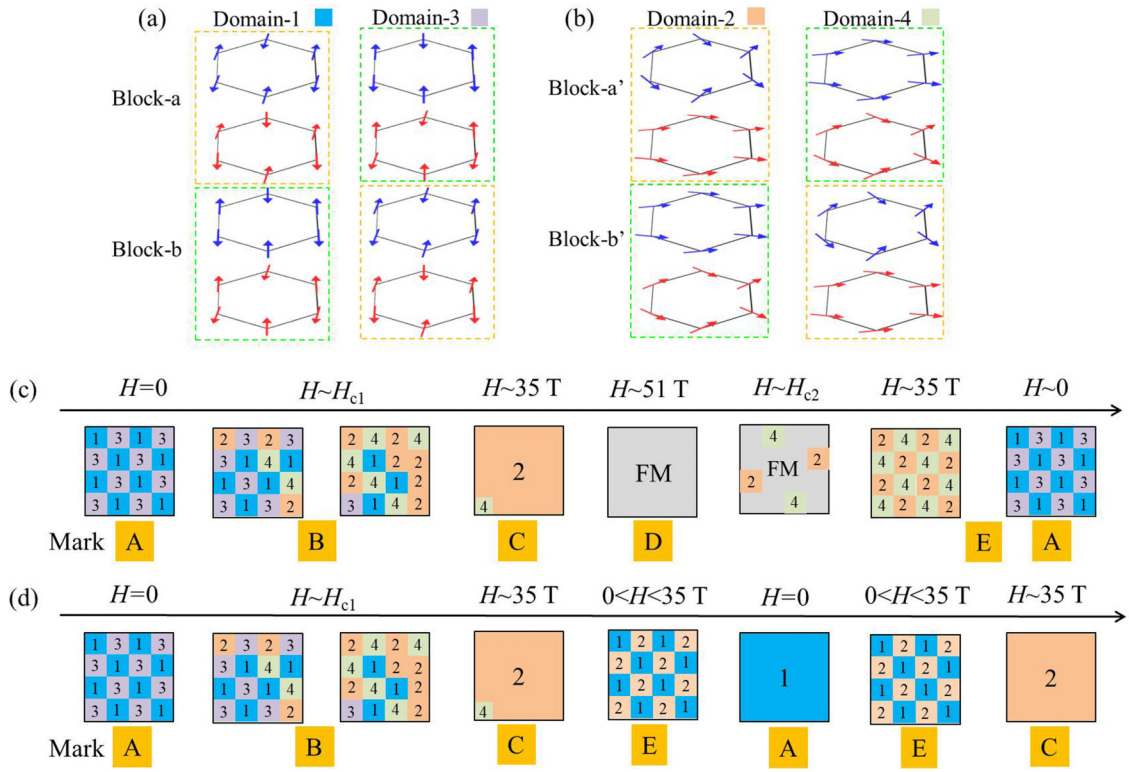

FIG. 5. Sketch of (a) domain 1 and domain 3 in the initial state, and (b) domain 2 and domain 4 in the presence of magnetic field. (c) Possible domain evolution of the remarkable $P(H)$ hysteresis. (d) Possible domain evolution of the switching from the low-α to high α. Marks A–E indicate the positions with different P in the $P(H)$ curve in Fig. 1(e).

canting between the neighboring Co(2) rings is preserved. For both domain 2 and domain 4, electric polarization can arise along the twofold axis parallel to the [110] direction.

With this information obtained from the neutron-scattering experiments [28,29], we are now able to explain the $P(H)$ hysteresis in the present work. The initial state was obtained by cooling the sample from $T \gg T_N$ under $H = 0$ and $E = 0$. In this sense, diverse AFM domains coexist in the initial state, and they have different orientations. For instance, domains consisting of block a and block b have their neighboring units that are, respectively, generated by 120° and 240° rotations, and these units fill the whole sample. Because of the character of multidomain structure, the spin flopping driven by $H//[110]$ is relatively slow, and the ME response is weak, and thus one observes $\alpha \sim 4$ ps/m until H increasing up to H_{c1} and beyond.

As $H > H_{c1}$, the domains are rapidly merged by aligning the AFM components perpendicular to H, giving rise to the drastic enhancement in P and thus the maximal $P_m \sim 950\ \mu C/m^2$ at $\mu_0 H_{max} \sim 33$ T. Simultaneously, one assumes that in a sufficiently large region, block a′ and block b′ are stacked properly to fulfill the exchange interactions as mentioned above, driven by the reduction of domain-wall energy. In this stage, the system becomes dominated by a single-domain state, i.e., domain 2 or domain 4.

Now there are two subsequent paths to proceed: (1) Further increasing H till the complete FM state is reached ($H > H_{c2}$) and then back to the zero field. (2) Return-decreasing H back to the zero-field state from the dominant single-domain state. It will be shown that the two different paths result in two different zero-field states responsible for the ME memory effect.

(1) Further increasing H beyond H_{c2} stabilizes the FM domain over the whole sample, accompanied with the disappearance of polarization P. Subsequently, a return cycle from the FM domain structure with decreasing H would destabilize the FM domains, and AFM nuclei would appear in the FM matrix when H is lower than H_{c2}. It should be noted that these AFM nuclei can be domain-2 and domain-4 ones, which are generated in a random manner. They grow individually and gradually till $H \sim H_{max}$, at which these domains meet and occupy the whole sample and polarization P reaches the maximal value P_m. Importantly, massive domain walls (i.e. -a′-b′-b′-a′-) are expected. Further decreasing of H to zero from H_{max} is accompanied with the gradual release of the tilting of Co moments, while the AFM components remain perpendicular to $H//[110]$. This return path must be accompanied with the high-ME response ($\alpha \sim 40$ ps/m). Eventually, the sample almost returns back to the initial state where various domains coexist. This process is sketched in Fig. 5(c).

(2) Return-decreasing H from H_{max} where a single-domain state is dominant, drives the sample back to zero-field state via gradual rotation of the Co moments, leading to the high-ME response $\alpha \sim 40$ ps/m. However, the end state here is dominated by domain 1 with uniform stacking of -a-b-a-b-, different from the end state via path (1) where massive domain walls exist, as schematically shown in Fig. 5(d). Consequently, if one again increases $H//[110]$ from zero field, there would occur simply the transition from domain 1 ($-a-b-a-b-$) to domain 2 ($-a'-b'-a'-b'-$), and the sample exhibits the high-ME response $\alpha \sim 40$ ps/m.

To this stage, it is clear that two different states in the zero field appear for this system, depending on the H-cycle path. It should be mentioned that all the sequences and ME response as illustrated in the paper can be one by one reproduced by the above scenario, indicating on the other hand the validity of this scenario. Nevertheless, the proposed model is just as a first approach, and further comprehensive studies are desired to fully understand the linear-ME memory in $Co_4Nb_2O_9$.

V. CONCLUSION

In summary, linear ME memory has been realized in honeycomb antiferromagnet $Co_4Nb_2O_9$, which show high rigidity against external magnetic perturbations. The memory states are nonvolatile and possess very different linear ME coefficients for the high- and low-ME states, respectively. By applying electric field, the memory states can be switched safely, and the sign of ME coefficient is changed simultaneously. The AFM memory behaviors can be ascribed to the multiferroic domain evolution related to the inequivalent honeycomb lattices of Co ions. The concept of AFM linear-ME memory is appealing due to the possibility of designing low-power, fast-switching, and high-density deices.

ACKNOWLEDGMENTS

We acknowledge Dr. Huakun Zuo and Dr. Zengwei Zhu for help with magnetoelastic measurements. This work is supported by the National Nature Science Foundation of China (Grants No. 12174128, No. 12074135, No. 92163210, and No. 51721001), Hubei Province Natural Science Foundation of China (Grant No. 2020CFA083), and the Fundamental Research Funds for the Central Universities (Grants No. 2019kfyRCPY081 and 2019kfyXKJC010).

[1] S. Dong, J.-M. Liu, S.-W. Cheong, and Z. Ren, Adv. Phys. **64**, 519 (2015).
[2] S.-W. Cheong and M. Mostovoy, Nat. Mater. **6**, 13 (2007).
[3] T. Kimura, T. Goto, H. Shintani, K. Ishizaka, T. Arima, and Y. Tokura, Nature (London) **426**, 55 (2003).
[4] W. Eerenstein, N. D. Mathur, and J. F. Scott, Nature (London) **442**, 759 (2006).
[5] H. Schmid, Ferroelectrics **161**, 1 (1994).
[6] J. P. Rivera, Ferroelectrics **161**, 165 (1994).
[7] M. Fiebig, J Phys. D: Appl. Phys. **38**, R123 (2005).
[8] J. X. Shen, D. S. Shang, Y. S. Chai, S. G. Wang, B. G. Shen, and Y. Sun, Adv. Mater. **30**, 1706717 (2018).
[9] S.-P. Shen, D.-S. Shang, Y.-S. Chai, and Y. Sun, Chin. Phys. B **25**, 027703 (2016).
[10] T. Kosub, M. Kopte, R. Hühne, P. Appel, B. Shields, P. Maletinsky, R. Hübner, M. O. Liedke, J. Fassbender, O. G. Schmidt, and D. Makarov, Nat. Commun. **8**, 13985 (2017).

[11] A. Malashevich, S. Coh, I. Souza, and D. Vanderbilt, Phys. Rev. B **86**, 094430 (2012).
[12] E. Bousquet, N. A. Spaldin, and K. T. Delaney, Phys. Rev. Lett. **106**, 107202 (2011).
[13] A. Scaramucci, E. Bousquet, M. Fechner, M. Mostovoy, and N. A. Spaldin, Phys. Rev. Lett. **109**, 197203 (2012).
[14] D. Ielmini and H. S. P. Wong, Nat. Electron. **1**, 333 (2018).
[15] R. Berdan, T. Marukame, K. Ota, M. Yamaguchi, M. Saitoh, S. Fujii, J. Deguchi, and Y. Nishi, Nat. Electron. **3**, 259 (2020).
[16] E. Ascher, H. Rieder, H. Schmid, and H. Stössel, J Appl. Phys. **37**, 1404 (1966).
[17] T. Kurumaji, S. Ishiwata, and Y. Tokura, Phys. Rev. B **95**, 045142 (2017).
[18] T. Kurumaji, S. Ishiwata, and Y. Tokura, Phys. Rev. X **5**, 031034 (2015).
[19] T. Arima, D. Higashiyama, Y. Kaneko, J. P. He, T. Goto, S. Miyasaka, T. Kimura, K. Oikawa, T. Kamiyama, R. Kumai, and Y. Tokura, Phys. Rev. B **70**, 064426 (2004).
[20] A. S. Zimmermann, D. Meier, and M. Fiebig, Nat. Commun. **5**, 4796 (2014).
[21] V. Kocsis, Y. Tokunaga, Y. Tokura, and Y. Taguchi, Phys. Rev. B **104**, 054426 (2021).
[22] Y. Yamasaki, H. Sagayama, T. Goto, M. Matsuura, K. Hirota, T. Arima, and Y. Tokura, Phys. Rev. Lett. **98**, 147204 (2007).
[23] V. Baltz, A. Manchon, M. Tsoi, T. Moriyama, T. Ono, and Y. Tserkovnyak, Rev. Mod. Phys. **90**, 015005 (2018).
[24] T. Jungwirth, X. Marti, P. Wadley, and J. Wunderlich, Nat. Nanotechnol. **11**, 231 (2016).
[25] X. Marti, I. Fina, C. Frontera, J. Liu, P. Wadley, Q. He, R. J. Paull, J. D. Clarkson, J. Kudrnovský, I. Turek, J. Kuneš, D. Yi, J-H. Chu, C. T. Nelson, L. You, E. Arenholz, S. Salahuddin, J. Fontcuberta, T. Jungwirth, and R. Ramesh, Nat. Mater. **13**, 367 (2014).
[26] E. F. Bertaut, L. Corliss, F. Forrat, R. Aleonard, and R. Pauthenet, J Phys. Chem. Solids **21**, 234 (1961).
[27] Y. Fang, Y. Q. Song, W. P. Zhou, R. Zhao, R. J. Tang, H. Yang, L. Y. Lv, S. G. Yang, D. H. Wang, and Y. W. Du, Sci. Rep. **4**, 3860 (2014).
[28] L. Ding, Minseong Lee, T. Hong, Zhiling Dun, R. Sinclair, S. X. Chi, H. K. Agrawal, E. S. Choi, B. C. Chakoumakos, H. D. Zhou, and H. B. Cao, Phys. Rev. B **102**, 174443 (2020).
[29] G. Deng, Y. Cao, W. Ren, S. Cao, A. J. Studer, N. Gauthier, M. Kenzelmann, G. Davidson, K. C. Rule, J. S. Gardner, P. Imperia, C. Ulrich, and G. J. McIntyre, Phys. Rev. B **97**, 085154 (2018).
[30] N. D. Khanh, N. Abe, H. Sagayama, A. Nakao, T. Hanashima, R. Kiyanagi, Y. Tokunaga, and T. Arima, Phys. Rev. B **93**, 075117 (2016).
[31] N. D. Khanh, N. Abe, K. Matsuura, H. Sagayama, Y. Tokunaga, and T. Arima, Appl. Phys. Lett. **114**, 102905 (2019).
[32] N. D. Khanh, N. Abe, S. Kimura, Y. Tokunaga, and T. Arima, Phys. Rev. B **96**, 094434 (2017).
[33] I. V. Solovyev and T. V. Kolodiazhnyi, Phys. Rev. B **94**, 094427 (2016).
[34] See Supplemental Material at http://link.aps.org/supplemental/10.1103/PhysRevB.107.014412 for URL for the full data of pulsed high magnetic-field measurements.